



**HAL**  
open science

## Mode-enhanced space-time DIC: Applications to ultra high-speed imaging

Myriam Berny, Clément Jailin, Amine Bouterf, François Hild, Stephane Roux

► **To cite this version:**

Myriam Berny, Clément Jailin, Amine Bouterf, François Hild, Stephane Roux. Mode-enhanced space-time DIC: Applications to ultra high-speed imaging. *Measurement Science and Technology*, 2018, 29 (12), pp.125008. 10.1088/1361-6501/aae3d5 . hal-01878095

**HAL Id: hal-01878095**

**<https://hal.science/hal-01878095v1>**

Submitted on 20 Sep 2018

**HAL** is a multi-disciplinary open access archive for the deposit and dissemination of scientific research documents, whether they are published or not. The documents may come from teaching and research institutions in France or abroad, or from public or private research centers.

L'archive ouverte pluridisciplinaire **HAL**, est destinée au dépôt et à la diffusion de documents scientifiques de niveau recherche, publiés ou non, émanant des établissements d'enseignement et de recherche français ou étrangers, des laboratoires publics ou privés.

# Mode-enhanced space-time DIC: Applications to ultra high-speed imaging

Myriam Berny,<sup>1,2</sup> Clément Jailin,<sup>1</sup> Amine Bouterf,<sup>1</sup>

François Hild<sup>1,\*</sup> and Stéphane Roux<sup>1</sup>

<sup>1</sup>Laboratoire de Mécanique et Technologie (LMT)

ENS Paris-Saclay / CNRS / University Paris-Saclay, Cachan, France

<sup>2</sup>SAFRAN, Safran Ceramics, Le Haillan, France

\*Corresponding author. Email: francois.hild@ens-paris-saclay.fr

**Abstract.** Digital Image Correlation (DIC), which consists in registering image pairs to measure displacement fields, can be tailored to analyze image sequences from videos taking advantage of a common reference image. In the present study it is no longer the first image of the sequence but rather a computed image from the entire video. The sought kinematics, which is separated in space and time, offers the opportunity to extract “modes,” each of which is a spatial displacement field multiplied by a scalar function of time only. These modes are not chosen a priori but rather computed from a specific formulation of DIC so that they capture the displacements at best. The exploited mathematical technique to achieve this modal representation is a form of Proper Generalized Decomposition (PGD) that makes use of the DIC variational formulation, where both spatial and temporal regularizations can be included. Two image videos acquired with an ultra-high speed camera at 5 and 10 million frames per second are analyzed to illustrate the proposed technique. Very large computation time gains are obtained with no noticeable differences in the kinematic measurements. Moreover, it is shown that motions have a lower complexity, *i.e.*, require less modes, than the direct Proper Orthogonal Decomposition (or Principal Component Analysis)

performed on the entire video.

**Keywords:** Brazilian test, Global DIC, Proper Generalized Decomposition, Proper Orthogonal Decomposition, Space-time analyses, Ultra-high speed camera

Submitted to: *Meas. Sci. Technol.*

## 1. Introduction

Digital Image Correlation (DIC) is being more and more used to measure 2D, 3D surface and volume displacements [1, 2, 3]. In its 2D and instantaneous version, DIC consists in registering two images by evaluating displacement fields that yield the best possible match. The analyzed image series, usually with instantaneous formulations, are often obtained by utilizing either conventional or high speed cameras. High-speed photography of laser and white light speckles [4, 5, 6], and DIC [7] were utilized to study dynamic tests in the 1980s. For example, stress intensity factors were evaluated and favorably compared with estimations using caustics [7]. With the development of digital high-speed cameras, 2D-DIC has become popular for monitoring dynamic tests since the turn of the century (see *e.g.*, Refs. [8, 9, 10, 11, 12, 13, 14, 15]). To illustrate the application of the proposed approach and reveal its advantages, image series acquired with an ultra-high speed camera at 5 and 10 million frames per second (fps) are chosen. These two cases belong to the category of images with some of the fastest rates that are available today and may therefore be more demanding in terms of image noise and overall quality than under standard imaging conditions.

In its early developments, DIC consisted in registering zones of interest or ZOIs (*i.e.*, small interrogation windows [16, 17, 18]) in the considered Region of Interest (ROI). This type of approach is now referred to as *local* (*i.e.*, the only information that is kept is the mean displacement assigned to each analyzed ZOI center) and instantaneous since only two pictures are considered. Each registration is performed over the ZOI area with various kinematic hypotheses, possibly accounting for their warping. In global and instantaneous approaches, which appeared more recently [19, 20, 21, 22], the registration is performed over the whole ROI. In the following developments, a

finite element formulation of DIC will be considered. Although initially introduced with regular meshes made of 4-noded quadrilaterals to comply with the pixel matrix (*i.e.*, Q4-DIC [22]), unstructured meshes based on, say, 3-noded triangles revealed more convenient to accurately follow sample boundaries (*i.e.*, T3-DIC [23]). The advantage of finite element formulations is their direct link with numerical simulations of mechanical problems for which the very same discretization may be considered [23, 24]. Moreover, displacement continuity (and possibly higher order regularity if needed) naturally results in contrast with local approaches.

As a way to reduce the complexity of measured fields, the Proper Orthogonal Decomposition (POD) (and related techniques known as singular value decomposition (SVD), principal component analysis (PCA), Karhunen-Loève (KL) transforms), revealed very powerful by truncating the description of the field of interest to the most salient modes [25, 26]. These approaches have two goals. First, reduction of measured data can relate to a denoising procedure [27]. The authors used the POD technique to preprocess a series of noisy thermal fields in order to filter out principal modes and then assess heat sources. Second, these techniques are used to reduce the huge amount of data, condense and simplify them, which is relevant when dealing with images of hierarchical complex materials [28] or with numerous and redundant sensor data [29]. Images can also be processed through model reduction techniques in order to assess the best location for sensors and condense information to key points [30]. It is therefore very appealing to consider such an approach in the context of DIC or DVC as a way to reduce large series of images to key data. Very recently, thermomechanical space-time simulations were processed through Karhunen-Loève decomposition to extract dominant temporal and spatial modes [31]. The temporal modes were then inserted in a spatiotemporal DIC framework to estimate the experimental spatial modes that

account for both gray level variations (and hence temperature) and displacement fields.

When the fields are not simply considered as data, but rather as originating from a known model, an extension of POD can be used, which is known as the Proper Generalized Decomposition (PGD) [32, 33, 34, 35] where modes are computed from the equation to solve in order to optimally reduce the discrepancy between the actual solution and its current approximation. Because the influence of each mode is often nonlinear, PGD proceeds following a “greedy” approach [36] where few (in particular one) mode(s) are added at each iteration. Approaches such as PGD, Discrete Empirical Interpolation Method (DEIM) or Kalman filters, all based on the generating model, are efficient to handle big data and sample the parametric space, especially for real-time monitoring of structures and data assimilation [37, 38].

The idea of using such possibilities in the context of DIC has prompted Passieux *et al.* to consider the PGD method for 2D-DIC [39] and later on for 3D-DVC [40]. The authors used a separated representation of the displacement field along the different spatial directions. Although this pioneering work led to an elegant formulation and solutions of high quality, the efficiency of the code revealed somewhat disappointing as compared to the initial ambition. Very recently, PGD-stereoDIC was extended to space time analyses [41]. A very strong time regularization was chosen in the form of one vibrational mode. A fixed point algorithm was implemented. Another implementation will be considered hereafter and more temporal modes will be constructed.

Reduction techniques can also be introduced to post-process DIC data and construct reduced models for better and simpler calibration of material parameters [42]. Last, Integrated-DIC procedures [43, 44, 24] can also be seen as a model reduction technique to identify parameters directly from gray level images.

In the present work, a model reduction technique (*i.e.*, the PGD framework) is

followed in the context of spatiotemporal DIC analyses for displacement assessments where space and time variables are separated [45, 35]. The fact that images generally have a smooth history in time and where the main spatial features are preserved from one frame to the next, if not over the entire series, makes the approach extremely efficient. Thus the initially limiting point is not the PGD technique by itself, but rather the dimensions over which a tensorial representation is sought. However, because all spatial dimensions are kept together without separation, the problem requires a different setting than that introduced in Refs. [39, 40], and is closer to other spacetime frameworks [46, 47, 41].

It is also worth emphasizing that the same spirit has also been used very recently in 4D-DVC (*i.e.*, dealing with 3D space and 1D time displacement fields), also separating time from space [48]. Here again, this PGD approach revealed extremely rewarding. However, it was developed for a very particular DVC procedure, called P-DVC, where the kinematics is read from few tomographic projections. It required specific developments that cannot simply be transposed from the present setting. Hence, although the general philosophy has been used sometimes in the context of DIC or DVC, possibly within sophisticated frameworks, the plain PGD strategy applied to space and time separation in 2D-DIC is the motivation of the present study.

Although the spirit of the approach developed in Ref. [41] is close to the method proposed herein, some very general differences are worth being emphasized:

- *regularization, i.e.*, introducing an additional cost function to favor the smoothness or mechanical admissibility of displacement fields is shown to be compatible with the determination of dominant modes. Let us stress that the temporal regularization is very intimately associated with the determination of eigen-modes through a change of metric that, to the best of the authors' knowledge, is original in the context of PGD.

- The *reference state* is not (as usual) the first image in the time series but it is computed from the determination of the kinematics. This peculiar formulation is not specific to PGD-DIC [47] but is introduced here and shown to be fully compatible with the proposed methodology.
- The *connection* of this approach with a POD decomposition of the image stack is shown to be very intimate in the limit of a vanishing displacement amplitude. However, for large displacements, pixel-wise extrapolation nonlinearities set in and lead to a much better suited (from its physically motivated roots) methodology for data reduction.
- Other technical details, such as the way multiple modes are handled, will become more transparent after the detailed presentation of the algorithm in the following section.

Section 2 presents the problem and the specific PGD formulation. The general setting of space-time DIC, then space-time separation of the displacement parameterization, and finally the PGD framework are introduced. Time and space regularization strategies are discussed. The details of the implementation are described in Section 3 including the regularization strategy and the construction of a denoised reference picture. As already noted [46, 47, 41], non intrusive implementations can be proposed. Section 4 considers two test cases that consist of cylindrical specimen fractured under high speed impact in diametral compression. These demanding test cases, which were captured at 5 and 10 Mfps, display different degrees of complexity. In both cases, the PGD approach leads to very significant gains in computation times. Finally, considering these examples, the relationship between PGD-DIC and a direct POD analysis of the image sequence is discussed to highlight the relationship between both approaches and the additional benefit of the proposed PGD-DIC.



## 2. Methodology

### 2.1. Spatiotemporal DIC Framework

An experiment leads to the acquisition of series of images  $f(\mathbf{x}, t)$ , where  $\mathbf{x}$  is any pixel position in the picture, and  $t$  the considered time. What is sought is the kinematics that is assumed to relate all images through gray level conservation [1, 2]

$$f(\mathbf{x} + \mathbf{u}(\mathbf{x}, t), t) = \hat{f}(\mathbf{x}) + \eta(\mathbf{x}, t) \quad (1)$$

where  $\eta$  is the noise corrupting images, and  $\mathbf{u}$  the actual displacement field. In the following, the noise will be assumed to be white and Gaussian, hence

$$\langle \eta(\mathbf{x}, t) \eta(\mathbf{x}', t') \rangle = \sigma^2 \delta(\mathbf{x} - \mathbf{x}') \delta(t - t') \quad (2)$$

where  $\langle \dots \rangle$  denote space and time averages, and  $\delta$  Kronecker operator. The reference state,  $\hat{f}(\mathbf{x})$ , is chosen to be given by the initial configuration at  $t_0$ , so that by definition,

$$\mathbf{u}(\mathbf{x}, t_0) = \mathbf{0} \quad (3)$$

Unfortunately, because of noise,  $\hat{f}(\mathbf{x})$  is not equal to  $f(\mathbf{x}, t_0)$ . Actually, it is unknown, and has to be determined. This is one challenge of the problem.

For any trial displacement field in space and time,  $\mathbf{v}(\mathbf{x}, t)$ , the corrected image  $\tilde{f}_{\mathbf{v}}$  reads

$$\tilde{f}_{\mathbf{v}}(\mathbf{x}, t) = f(\mathbf{x} + \mathbf{v}(\mathbf{x}, t), t) \quad (4)$$

and the gray level residual  $\rho$  is defined as

$$\rho[\mathbf{v}](\mathbf{x}, t) = \tilde{f}_{\mathbf{v}}(\mathbf{x}, t) - \hat{f}(\mathbf{x}) \quad (5)$$

Ideally, at convergence,  $\mathbf{v} \equiv \mathbf{u}$ , and  $\rho$  should coincide with the noise  $\eta$ . Thus, the maximization of the log-likelihood leads to the minimization of the following cost function [49]

$$\mathfrak{T}[\mathbf{v}] = \frac{1}{N_t N_x \sigma^2} \|\rho\|^2 \quad (6)$$

where the prefactor is chosen for normalization purposes, namely,  $\langle \mathfrak{I}[\mathbf{u}] \rangle = 1$ , when  $N_t$  is the number of frames, and  $N_x$  the number of pixels of the ROI. Here  $\|\dots\|^2$  is the Euclidean L2-norm, since noise is assumed to be white (independent) Gaussian and identically distributed (iid).

The displacement field  $\mathbf{v}(\mathbf{x}, t)$  is assumed to be parameterized with (a priori chosen) spatiotemporal fields  $\Upsilon_i$

$$\mathbf{v}(\mathbf{x}, t) = \sum_i v_i \Upsilon_i(\mathbf{x}, t) \quad (7)$$

and the unknown amplitudes  $v_i$  have to be determined. Computing the gradient of the linearized cost function and assuming that  $\nabla \tilde{f}_v \approx \nabla \hat{f}$

$$\frac{\partial \mathfrak{I}}{\partial \delta v_i} = \frac{2}{N_t N_x \sigma^2} \sum_{\mathbf{x}} \sum_{t=1}^{N_t} \rho[\mathbf{v}](\mathbf{x}, t) (\nabla \hat{f}(\mathbf{x}) \cdot \Upsilon_i(\mathbf{x}, t)) \quad (8)$$

with respect to the corrections  $\delta v_i$  to the amplitude  $v_i$  and its Hessian

$$\frac{\partial^2 \mathfrak{I}}{\partial \delta v_i \partial \delta v_j} = \frac{2}{N_t N_x \sigma^2} \sum_{\mathbf{x}} \sum_{t=1}^{N_t} (\nabla \hat{f}(\mathbf{x}) \cdot \Upsilon_i(\mathbf{x}, t)) (\nabla \hat{f}(\mathbf{x}) \cdot \Upsilon_j(\mathbf{x}, t)) \quad (9)$$

leads to the following formulation for the correction  $\delta v_j$

$$\begin{aligned} \sum_{\mathbf{x}} \sum_{t=1}^{N_t} \left[ (\nabla \hat{f}(\mathbf{x}) \cdot \Upsilon_i(\mathbf{x}, t)) (\nabla \hat{f}(\mathbf{x}) \cdot \Upsilon_j(\mathbf{x}, t)) \right] \delta v_j = \\ = - \sum_{\mathbf{x}} \sum_{t=1}^{N_t} \rho[\mathbf{v}](\mathbf{x}, t) (\nabla \hat{f}(\mathbf{x}) \cdot \Upsilon_i(\mathbf{x}, t)) \end{aligned} \quad (10)$$

## 2.2. PGD implementation

The displacement field  $\mathbf{v}(\mathbf{x}, t)$  is written in a separated form [45, 50, 51], which is natural in the present context and not restrictive

$$\mathbf{v}(\mathbf{x}, t) = \sum_{ij} a_{ij} \phi_i(\mathbf{x}) \psi_j(t) \quad (11)$$

Well-posedness results from an appropriate selection of the above introduced spatial fields,  $\phi_i(\mathbf{x})$  (e.g., spatial finite element shape functions) and time basis functions  $\psi_j(t)$ . The principle of PGD is to incorporate few “modes” along the iterations [25,

32, 33, 34, 35]. Each mode is separated in space and time so that the space field is  $\boldsymbol{\varphi}(\mathbf{x}) = \sum_i b_i \boldsymbol{\phi}_i(\mathbf{x})$ , the time dependence is  $\chi(t) = \sum_j c_j \psi_j(t)$ , and the displacement field reads  $\mathbf{v} = a\boldsymbol{\varphi}(\mathbf{x})\chi(t)$ , where  $a$  denotes the sought amplitude. Inserting one such mode into Equation (10) gives

$$\begin{aligned} & \left[ \sum_t^{N_t} \chi(t)^2 \right] \left[ \sum_{\mathbf{x}}^{N_x} \left( \boldsymbol{\varphi}(\mathbf{x}) \cdot \nabla \hat{f}(\mathbf{x}) \right)^2 \right] \delta a = \\ & = - \sum_t^{N_t} \sum_{\mathbf{x}}^{N_x} \rho(\mathbf{x}, t) \chi(t) \left( \boldsymbol{\varphi}(\mathbf{x}) \cdot \nabla \hat{f}(\mathbf{x}) \right) \end{aligned} \quad (12)$$

The amplitudes  $b_i$  and  $c_j$  can be chosen so that the space field and the time function are normalized

$$\begin{aligned} \sum_{\mathbf{x}}^{N_x} \left( \boldsymbol{\varphi}(\mathbf{x}) \cdot \nabla \hat{f}(\mathbf{x}) \right)^2 &= 1 \\ \sum_t^{N_t} \chi(t)^2 &= 1 \end{aligned} \quad (13)$$

To maximize the benefit of this single mode, the space and time dependencies are to be optimized. Reverting to the osculating quadratic potential of the cost function, its decrease,  $\Delta$ , is proportional to

$$\Delta = \left[ \sum_{\mathbf{x}, t} \rho(\mathbf{x}, t) \chi(t) \left( \boldsymbol{\varphi}(\mathbf{x}) \cdot \nabla \hat{f}(\mathbf{x}) \right) \right]^2 \quad (14)$$

The first mode of the SVD of  $\rho(\mathbf{x}, t) = r\alpha(\mathbf{x})\beta(t) + h.o.t.$  (where  $\alpha$  is the spatial eigenvector, and  $\beta$  the temporal one, and  $r$  the eigenvalue) solves this problem in the sense that  $\chi(t) \propto \beta(t)$  and  $\left( \boldsymbol{\varphi}(\mathbf{x}) \cdot \nabla \hat{f}(\mathbf{x}) \right) \propto \alpha(\mathbf{x})$ . Using the normalization conditions, the above proportionalities are in fact equalities (up to sign conventions). Thus the time history is entirely determined. However, the displacement field is not. This is due to the fact that only the displacement component that is aligned with the gray level gradient is constrained. All displacements fields that would be tangent to iso-contours of the gray level pattern never come into play in DIC. One of the reasons to have a very fine speckle pattern is to make sure that those fields are nonphysical.

In order to solve this problem, one strategy is to measure  $\alpha$  with the highest definition, that is pixel-wise, but keep the displacement field with a coarser resolution. Writing  $\varphi(\mathbf{x}) = \sum_i b_i \phi_i(\mathbf{x})$ , one may seek the set of amplitudes gathered in the column-vector  $\{\mathbf{b}\}$  that minimizes the quadratic distance to  $\alpha$ . Thus a cost function  $\mathfrak{P}$  is introduced

$$\mathfrak{P}[\{\mathbf{b}\}] = \sum_{\mathbf{x}} \left( \sum_i b_i \phi_i(\mathbf{x}) \cdot \nabla \hat{f}(\mathbf{x}) - \alpha(\mathbf{x}) \right)^2 \quad (15)$$

leading to

$$\sum_{\mathbf{x}} \left( \sum_j b_j \phi_j(\mathbf{x}) \cdot \nabla \hat{f}(\mathbf{x}) - \alpha(\mathbf{x}) \right) \left( \phi_i(\mathbf{x}) \cdot \nabla \hat{f}(\mathbf{x}) \right) = 0 \quad (16)$$

or equivalently

$$[\mathbf{M}]\{\mathbf{b}\} = \{\mathbf{m}\} \quad (17)$$

with

$$\begin{aligned} M_{ij} &= \sum_{\mathbf{x}} (\phi_i(\mathbf{x}) \cdot \nabla \hat{f}(\mathbf{x})) (\phi_j(\mathbf{x}) \cdot \nabla \hat{f}(\mathbf{x})) \\ m_i &= \sum_{\mathbf{x}} (\phi_i(\mathbf{x}) \cdot \nabla \hat{f}(\mathbf{x})) \alpha(\mathbf{x}) \end{aligned} \quad (18)$$

It is noteworthy that  $[\mathbf{M}]$  is exactly the standard DIC matrix [2], and solving the above equation for  $\{\mathbf{b}\}$  is exactly one classical DIC iteration if  $\alpha$  is interpreted as a residual field. Actually this is the case since it is the spatial mode of a spatiotemporal residual  $\rho$ . Thus it appears that for the present problem, PGD reduces to a mere POD decomposition of the residual field over time, where each mode feeds an instantaneous DIC analysis. This equivalence does not come as a surprise since the time dimension plays no specific role in the DIC problem. Yet, the incorporation of such a modal approach in spatiotemporal DIC frameworks brings a number of advantages, detailed below, and as shown in Section 5, it differs significantly from a simple POD decomposition of images (unless the displacement amplitude is so low that

the motion can be accurately described with the image gradient). When one single mode is considered [41], the residual first decreases, but soon reaches a steady level as it is progressively pushed into the kernel of the  $[\mathbf{M}]$  matrix. This does not mean that no additional information in  $\rho$  may be interpreted as due to displacements, but simply that the dominant mode for the residual is progressively exhausted. Consequently, more modes are to be considered. Thus, a number  $N_m$  of retained modes corresponding to the largest temporal eigenvalues is introduced.

### 2.3. Regularization

As seen above, PGD and POD are excellent ways to reduce the complexity of the problem in terms of degrees of freedom. However, neither specific smoothness nor regularity constraint were prescribed to the modes. Both low and high frequencies are expected to be present in the modes as called by the properties of the residuals. Consequently, noise sensitivity is expected to occur in particular for the temporal response [46]. It is proposed to mitigate such effects by considering either so-called soft or hard regularizations [52].

The philosophy of regularization is to reduce the number of degrees of freedom for better conditioning, or dampen their fluctuations by penalizing them, and from there results the benefit of designing the best fitted description involving the smallest number of parameters. The limit of this approach is that, without prior information, the range of considered displacement fields may be too limited to precisely account for the actual kinematics.

*2.3.1. Temporal regularization* This subsection addresses two possibilities to introduce such regularization, and the time dimension is considered first. The first route, which is referred to as “hard regularization,” consists in choosing a basis of functions in time, rich

enough to provide a fair representation of the actual time history but with the required regularity or smoothness. For instance linear [53] or tent shaped functions (*i.e.*, 1D regular linear finite elements [46, 47]) will provide  $\mathcal{C}_0$  continuity. Cubic splines provide a higher (*i.e.*,  $\mathcal{C}_2$ ) regularity. Band limited Fourier modes are also a convenient way to tune smoothness at will [41]. Let us call  $\psi_i(t)$ , the  $i = 1, \dots, M$  functions generating the space of admissible time variations. This basis, without restriction, can be considered as orthonormal with respect to the Euclidean scalar product

$$\sum_{t=1}^{N_t} \psi_i(t)\psi_j(t) = \delta_{ij} \quad (19)$$

The tensor

$$P(t, t') = \sum_i \psi_i(t)\psi_i(t') \quad \text{or} \quad [\mathbf{P}] = \{\boldsymbol{\psi}\} \cdot \{\boldsymbol{\psi}\}^\top \quad (20)$$

is thus an  $N_t \times N_t$  projector. Hence, a first poor-man solution consists in filtering the time modes as  $\{\tilde{\boldsymbol{\beta}}\} = [\mathbf{P}] \cdot \{\boldsymbol{\beta}\}$ . However, in so doing, the ranking of the modes inherited from the PGD procedure is lost. A better way consists in considering the PGD approach as would result from such a choice of temporal variations in the very root of the DIC formulation. It follows that the residual  $\rho(\mathbf{x}, t)$  would simply be filtered in time as  $\tilde{\rho}(\mathbf{x}, t) = \sum_{t'} P(t, t')\rho(\mathbf{x}, t')$ , from which the above PGD approach can be conducted, thereby leading to better suited modes.

In terms of implementation, since the number of pixels is generally much larger than the number of frames, *i.e.*,  $N_t \ll N_x$ , it is convenient to compute the temporal modes first, and derive the spatial modes afterward. Thus, with no time regularization, the temporal modes are the eigenvectors associated with the highest eigenvalues of the symmetric matrix  $R(t, t') = \sum_{\mathbf{x}} \rho(\mathbf{x}, t)\rho(\mathbf{x}, t')$ . To include regularization, it suffices to consider the dominant modes of  $[\tilde{\mathbf{R}}] = [\mathbf{P}] \cdot [\mathbf{R}] \cdot [\mathbf{P}]$ , that is a very cheap change, and it allows the regularization to be tuned with a very mild intrusiveness.

The second route, designated as “soft regularization,” rather than restricting abruptly the space in which  $\beta(t)$  is defined, proceeds through a more gradual penalty [52]. For instance, to limit high frequency variations in  $\beta(t)$ , they can be dampened by computing  $\gamma(t)$  such that

$$\mathfrak{S}[\gamma] = (1/2) \sum_t (\gamma(t) - \beta(t))^2 + \frac{\tau^2}{2} \sum_t \left( \frac{d\gamma}{dt} \right)^2 \quad (21)$$

is minimized. The first term of the sum, which corresponds to attachment to the data, binds  $\gamma$  to  $\beta$ , whereas the second term penalizes the rapid time fluctuations of  $\gamma$ . The  $\tau^2$  weight can be seen as the square of a time scale below which oscillations are filtered out (*i.e.*, the cut-off time of this low-pass filter). If the finite difference operator  $[\mathbf{D}]$  is introduced for the time derivative, the solution to the above minimization obeys

$$([\mathbf{I}] + \tau^2[\mathbf{D}]^\top[\mathbf{D}])\{\gamma\} = \{\beta\} \quad (22)$$

This observation prompts for the introduction of

$$[\mathbf{Q}] = ([\mathbf{I}] + \tau^2[\mathbf{D}]^\top[\mathbf{D}])^{-1} \quad (23)$$

such that  $\{\gamma\} = [\mathbf{Q}] \cdot \{\beta\}$ , where  $[\mathbf{I}]$  is the identity tensor. This notation emphasizes the analogy with hard regularization as the proximity of  $[\mathbf{P}]$  and  $[\mathbf{Q}]$ . The only difference is that  $[\mathbf{Q}]$  is no longer a projector. However it is also a symmetric operator and its eigenvalues lie within the interval  $[0; 1]$ , thus some modes may be dampened in the “soft” approach whereas they were either kept or suppressed in the “hard” regularization. As previously noted, the best way of introducing this regularization is to apply  $[\mathbf{Q}]$  to the residual prior to the PGD procedure, and thus it simply consists in considering the highest eigenvalues of  $[\tilde{\mathbf{R}}] = [\mathbf{Q}] \cdot [\mathbf{R}] \cdot [\mathbf{Q}]$ .

*2.3.2. Mechanical regularization* The same type of regularization could be performed over the spatial component. In particular, the “hard regularization” route can already be

read in the implementation of the finite element mesh. Having a coarse or fine mesh is a way to tune spatial regularity. However, changing the mesh is not a simple operation, and everything has to be coded anew, and for this reason, a “smooth regularization” is preferred as the mesh may remain unchanged.

Although the above formulation could be used, this was not the choice made herein, and an already existing DIC framework is utilized where the penalty functional is added to the DIC functional. The so-called equilibrium gap penalizes the displacement fields that deviate from being the solution to a homogeneous elastic problem [54, 55]. As compared to a plain DIC formulation, only the Hessian,  $[\mathbf{M}]$  (see Equation (18)), is modified by the addition of another symmetric matrix,  $[\mathbf{N}]$ , which is scaled by a weight that introduces a length scale,  $\xi$ , similar to the above  $\tau$  [56]. Because of this particular way of spatial regularization, no interference is made with the PGD approach that is computed on the second member (*i.e.*, the residual) only. The linearity of the DIC problem in the immediate vicinity of the solution guarantees that the superposition of regularized displacement fields will be itself a regularized field, and hence, it suffices to solve for the displacement field attached to each mode  $\alpha(\mathbf{x})$  with the appropriate regularized Hessian to generate the (spatially) regularized time history when weighted by the corresponding temporal eigen mode  $\beta$ .

### 3. Practical implementation

The implementation of the POD/PGD step is detailed in Algorithm 1. The denoised reference picture  $\hat{f}$  is gradually constructed as the PGD-based DIC scheme is iterated. It is obtained from the stack of pictures in the deformed configurations corrected by the measured displacement field  $\tilde{f}_v$ , all of these pictures being an estimation of  $\hat{f}$ . Because the whole stack is considered, random noise will be filtered out by considering the



temporal averages of these gray level pictures. In the present procedure, the reference image  $\hat{f}$  is not fully replaced by the time average of the corrected images. A parameter  $0 \leq \kappa \leq 1$  is introduced as an under-relaxation parameter in order to preserve the details in the reference image. Otherwise, an imperfect initial determination of the displacement would produce a slightly blurred  $\langle \tilde{f}_v \rangle_t$  that hampers or slows down the convergence to an accurate registration. In practice, a value of  $\kappa = 0.5$  will be used in the sequel. It is observed that, provided the two extreme values 0 and 1 are avoided, this parameter has a very weak sensitivity. Any value in the range [0.2; 0.8] could be chosen without any noticeable difference.

The regularization matrices  $[\mathbf{Q}]$  and  $[\mathbf{S}]$  are constructed in the initialization part of the algorithm making use of the regularization time  $\tau$  and length  $\xi$ . Their value can be set to 0 if no regularization is desired.

**Algorithm 1** PGD-DIC algorithm without regularization (neither temporal nor spatial)

---

```

1: procedure PGD-DIC ( $\mathbf{v}(x, t) \leftarrow \text{PGDDIC}(f(\mathbf{x}, t), \xi, \tau, \kappa)$ )
2:    $\hat{f}(\mathbf{x}) \leftarrow f(\mathbf{x}, t_0)$  ▷ Initialization
3:   Compute  $[\mathbf{S}]_\xi$  ▷ Mechanical regularization
4:   Compute  $[\mathbf{Q}]_\tau$  ▷ Temporal regularization
5:   while  $\|\delta\mathbf{v}\| > \epsilon_1$  and  $\|\delta\rho\| < -\epsilon_2$  do
6:      $\tilde{f}_v(\mathbf{x}, t) \leftarrow f(\mathbf{x} + \mathbf{v}(\mathbf{x}, t))$  ▷ Corrected image series
7:      $\hat{f}(\mathbf{x}) \leftarrow \kappa\hat{f}(\mathbf{x}) + (1 - \kappa)\langle \tilde{f}_v(\mathbf{x}, t) \rangle_t$  ▷ Reference image
8:      $\omega_i(\mathbf{x}) \leftarrow \phi_i(\mathbf{x}) \cdot \nabla \hat{f}(\mathbf{x})$ 
9:      $M_{ij} \leftarrow \sum_x \omega_i(\mathbf{x})\omega_j(\mathbf{x})$  ▷ DIC matrix
10:     $[\mathbf{M}] \leftarrow [\mathbf{M}] + [\mathbf{S}]_\xi$  ▷ Use mechanical regularization
11:     $\rho[\mathbf{v}](\mathbf{x}, t) \leftarrow \tilde{f}_v(\mathbf{x}, t) - \hat{f}(\mathbf{x})$  ▷ Residuals
12:     $R(t, t') \leftarrow \sum_x \rho[\mathbf{v}](\mathbf{x}, t)\rho[\mathbf{v}](\mathbf{x}, t')$ 
13:     $[\tilde{\mathbf{R}}] = [\mathbf{Q}]_\tau^\top [\mathbf{R}] [\mathbf{Q}]_\tau$  ▷ Use temporal regularization
14:    for  $n \leftarrow 1, N_m$  do
15:       $\beta_n(t) \leftarrow n\text{th largest eigenvectors of } [\tilde{\mathbf{R}}]$  ▷ Temporal mode
16:       $\alpha_n(\mathbf{x}) \leftarrow \sum_t \rho[\mathbf{v}](\mathbf{x}, t)\beta_n(t)$  ▷ Associated spatial mode
17:       $m_i \leftarrow \sum_x \alpha_n(\mathbf{x})\omega_i(\mathbf{x})$ 
18:       $b_i \leftarrow M_{ij}^{-1}m_j$ 
19:       $\delta\mathbf{v}(\mathbf{x}) \leftarrow \sum_i b_i\phi_i(\mathbf{x})$ 
20:       $\mathbf{v}(\mathbf{x}, t) \leftarrow \mathbf{v}(\mathbf{x}, t) + \delta\mathbf{v}(\mathbf{x})\beta_n(t)$ 
21:    end for
22:  end while
23:  return  $\mathbf{v}, \rho[\mathbf{v}]$  ▷ Displacement and residual
24: end procedure

```

---

It is interesting to note how modest the changes are for implementing the PGD version as compared to standard space-time versions of global DIC [46]. Few tens of Matlab code lines were needed to implement this variant. This non intrusiveness allows standard (stereo)DIC kernels to be used [47, 41]. To remove PGD from the previous algorithm, it suffices to consider in the “for” loop (*i.e.*, lines 14-21) a number of modes  $N_m$  equal to the number of temporal basis functions, and in this case the singular value decomposition that would be used as a mere change of basis is no longer needed.

In terms of convergence criteria, the first one is based on the incremental displacement that should be chosen less than the corresponding uncertainty (*e.g.*,  $\epsilon_1 = 10^{-3}$  pixel or smaller in the present case). Such a criterion is similar to that to be used in global and instantaneous DIC. It is chosen to be smaller than the uncertainty level, and as convergence is usually exponentially fast, with a typical decrease of such displacement changes by a decade over a few iteration, the sensitivity on this convergence criterion is rather low [2]. A second criterion is based on the decrease of the norm of gray level residual  $\|\delta\rho\|$  from one iteration to the next. When the residual is normalized by the dynamic range of the images (*i.e.*, gray level difference between maximum and minimum gray levels in the ROI), the minimum change is chosen to be  $10^{-4}$  in the following. This level is a standard practice for spacetime DIC [47] and is not specific to the PGD variant presented herein. Such a parameter is chosen very small (*i.e.*, less than the noise level) just as a safe detection of convergence, and choosing a smaller value increases the number of iterations without any detectable difference. Finally, an additional exit condition is implemented related to the maximum number of iterations. This is very usual for iterative algorithms in case they would not converge. This escape condition was never reached in the following cases.

#### 4. Test cases

To prove the feasibility and robustness of the present framework, Brazilian tests are considered. The Brazilian test is a simple indirect method to evaluate the tensile strength of brittle materials such as concrete and rocks [57, 58]. It consists in diametral compression of disks or cylinders that can be performed either quasi-statically or under dynamic loading conditions. In each test, a disk (72 mm in diameter and 10 mm in thickness) made of Ductal concrete was loaded up to failure under impact. The dynamic tests were carried out using Hopkinson bars (HB [59]) made of aluminum alloy (Figure 1). The HB system is composed of a pressurized air gun, a projectile 60 mm in diameter and 80 mm in length, an input bar with the same diameter and a length of 4500 mm, and an output bar with a length of 2000 mm. The test was carried out with a speed of the input bar equal to ca. 6 m/s. It is worth noting that in both tests, the observed sample surface has been patterned with black and white paint.

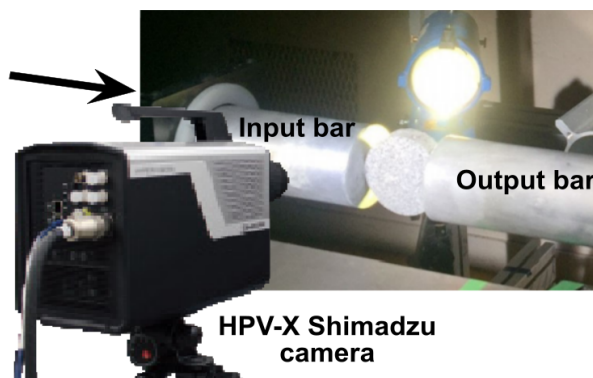


Figure 1: Brazilian test on Ductal concrete in Hopkinson bar setup (adapted from Ref. [60]). The black arrow indicates the direction of the incident wave.

One light spot (Dedolight) with maximum power of 400 W and two light heads (Dedocool) with maximum power of 250 W were switched on just before starting the tests to avoid heating. A Shimadzu HPV-X ultra-high speed camera was used to record the deformation of the specimen surface during HB tests. Image sequences with a definition of  $400 \times 250$  pixels were recorded. The lens used with the camera was a

50 mm Nikon F-Mount. The physical size of one pixel is  $360\ \mu\text{m}$ .

#### 4.1. 10 Mfps series

The first series is a sequence of 128 frames, which were acquired at a rate of 10 million frames per second. Figure 2 shows the first and last images of the series. The sequence started after the specimen had already been fractured. However, the DIC analysis reveals that a small amplitude motion took place in the captured interval, with mainly an opening of the main crack but also a secondary oblique crack located in the left part of the sample. The global amplitude of displacement is about one pixel (*i.e.*,  $360\ \mu\text{m}$ ).

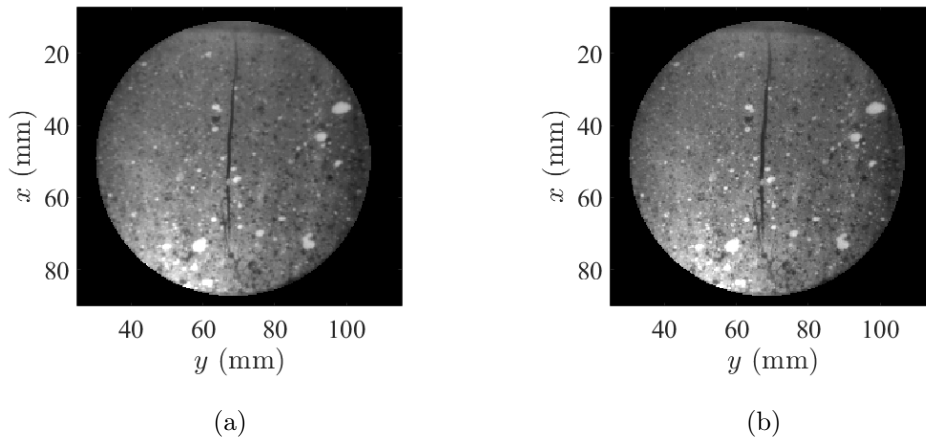


Figure 2: (a) Initial and (b) final image of the 10 Mfps series

The displacement is decomposed over a very fine unstructured mesh (Figure 3(a)) composed of T3 elements (*i.e.*, 3-noded triangles). The average size of triangle edges is 4 pixels. Mechanical regularization is introduced spatially with a length scale of 20 pixels. Time-wise, a time derivative is selected for regularization as above discussed (see Equation (23)), and the characteristic time is  $\tau = 10$  frames (or  $1\ \mu\text{s}$ ). The temporal modes obtained at the very last (*i.e.*, 7th) iteration are shown in Figure 3.

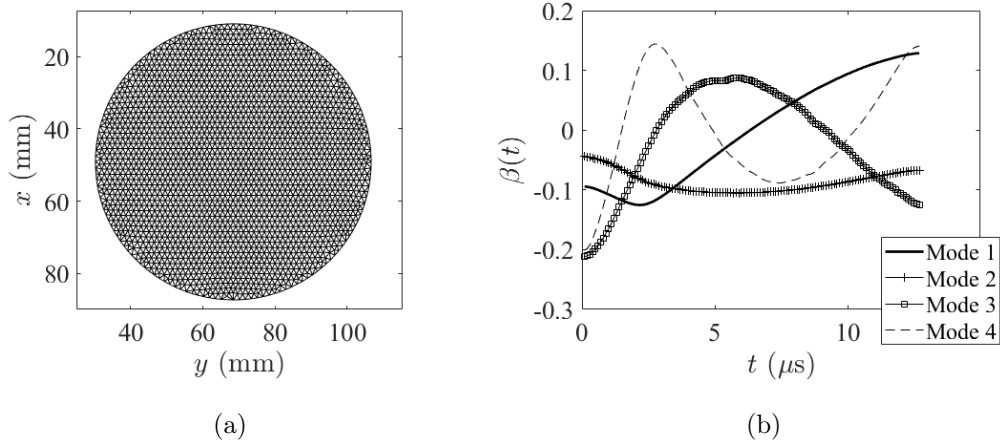


Figure 3: (a) Mesh used for the 10 Mfps series. The typical size of triangle edges is 4 pixels. (b) Time history of the four modes used at the final iteration

It is to be emphasized that since these modes do not vanish for the first frame, the displacement is not equal to 0 at this point. This is due to the fact that now the reference image is no longer identical to the first frame. It means in practice that the displacement field of the  $n$ th frame with respect to the first one has to be computed as the composition of the transformation from the  $n$ th image to the reference and from the reference to the 1st one. Optionally, the reference image could also be transported with the opposite of the displacement field of the first one so that their relative displacement be null. This route has not been followed in the present case and hence a small displacement is observed. The RMS displacement for the first image (with respect to the reference) is about 0.02 pixel (*i.e.*, 7  $\mu\text{m}$ ). It is also noteworthy that the first temporal modes (at the first iteration) were essentially polynomials of increasing order. The first mode was linear, the second was quadratic and so on. The absence of a polynomial of order 0 is expected as it would have to vanish at the origin of time and hence be null. Such a polynomial series can be compared for this example as a perturbative expansion because

of the small amplitude of motions, as discussed in the following section. In this analysis, no more than  $N_m = 4$  modes were needed.

As shown in Figure 4, the main mode is sample splitting into two halves, with an opening displacement of about 1 pixel (*i.e.*,  $360\ \mu\text{m}$ ) for  $u_y$ . Additionally,  $u_x$  reveals an oblique crack that propagates to the disk center. It cannot be noticed in the original images because of the very small opening (*i.e.*, about 0.1 pixel or equivalently  $36\ \mu\text{m}$ ).

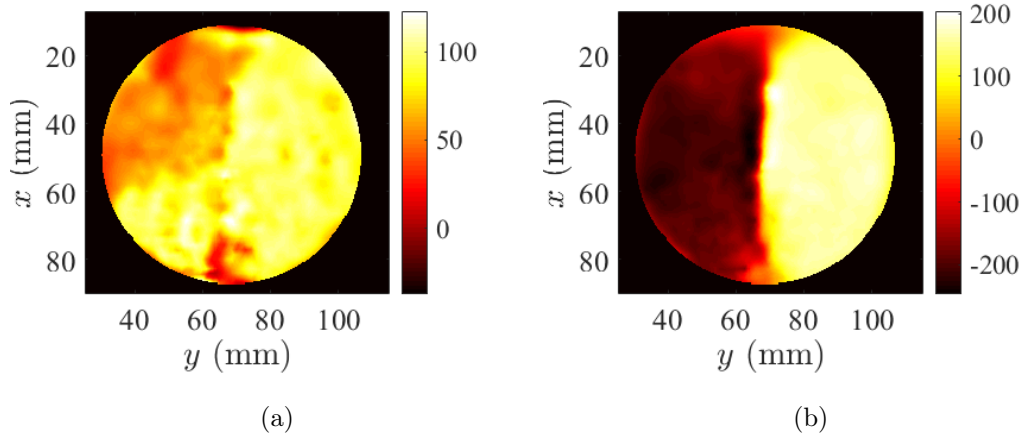


Figure 4: Displacement fields (expressed in  $\mu\text{m}$ ) at the last frame (a) along the vertical  $x$  direction and (b) horizontal  $y$  directions, for the 10 Mfps series

To illustrate the difficulty of the experiment, Figure 5 shows  $1.8\ \mu\text{s}$  after impact both the (horizontal) displacement and velocity fields. It is noteworthy that although the two main fragments begin to separate with a crack opening of the order of  $100\ \mu\text{m}$ , the velocity difference between the two parts is already in the  $100\ \text{m/s}$  range.

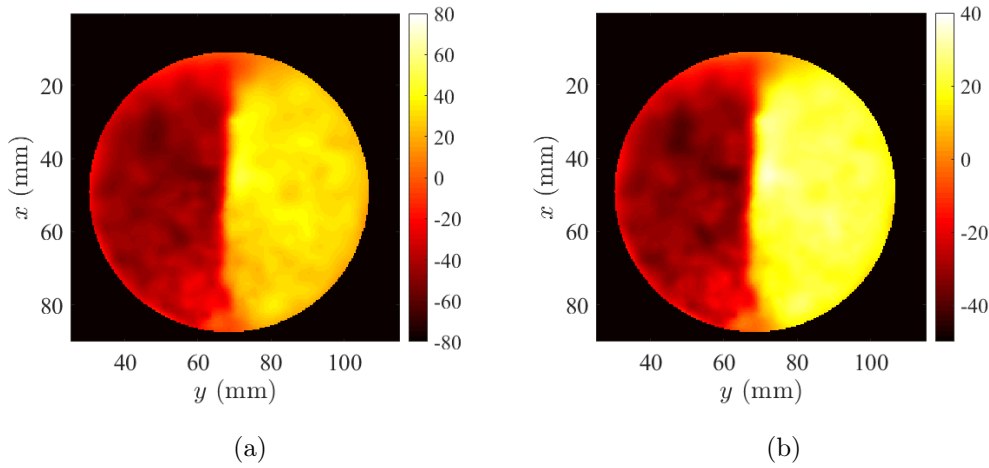


Figure 5: (a) Horizontal component of the displacement field (expressed in  $\mu\text{m}$ ) at  $t = 1.8 \mu\text{s}$ . (b) Corresponding velocity field (expressed in  $\text{m/s}$ )

The residuals (RMS of image differences) without displacement correction was quite modest, namely, 1.02 % of the gray level dynamic range  $\Delta f$ . However, after 7 iterations, the residuals constructed from the corrected images and the reference image that takes into account the entire series, were lowered down to 0.37 % of  $\Delta f$ . Such a level is to be stressed as it is very low for usual optical images [2], and here these images correspond to one of the fastest cameras available. Reaching such low values means that the noise level is remarkably low. Figure 6(a) shows the residuals on the final frame where the displacement is the largest. The main crack is easily visible as well as the crushing of the material at contact points. The secondary oblique crack is responsible for a very faint residual enhancement along its path, but without the observed displacement discontinuity, it would have been very difficult to assess.

Figure 6(b) shows a space-time field through the residual for a horizontal cut at mid sample height ( $x = 140$  pixels). Interestingly, although most part of the displacement field is increasing linearly from the first image on (see the mode 1 temporal variation in



Figure 3(b)) the minimum residual appears to be at about mid-time in the image series. The reason is due to the choice of the reference image as averaging over *all* corrected images. For instance, the crack opening itself cannot be captured by the displacement field that is continuous (only its influence away from the crack can be corrected). Thus, the crack in the reference image  $\hat{f}$  has to picture an opening that is intermediate between the initial and final states, and more or less coincides with that of the crack at mid-time interval. This has the effect of reducing the residual for this particular time at the expense of the early and late stages.

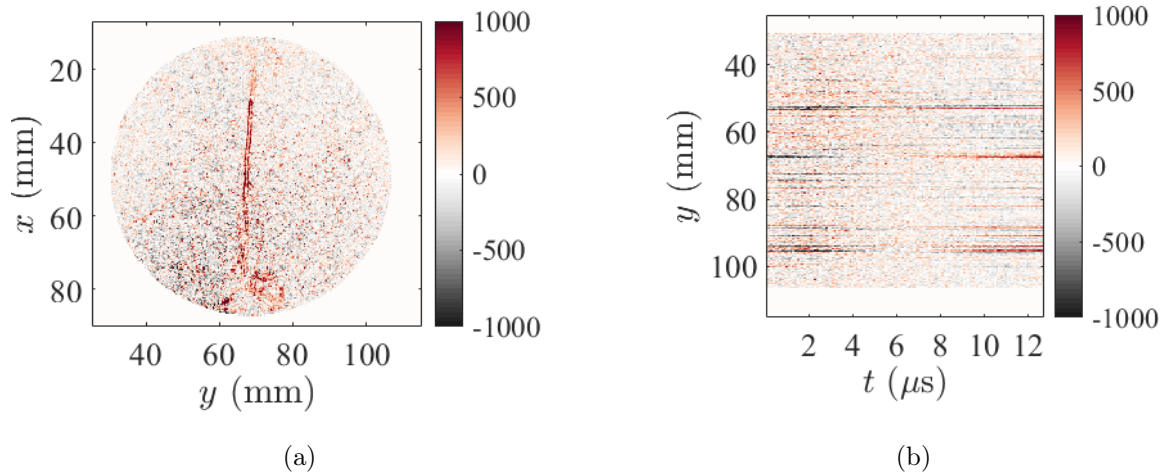


Figure 6: Gray level residuals field (a) for the last frame and (b) as a space-time cut at mid sample height for the 10 Mfps series. The dynamic range is  $\Delta f = 35000$  gray levels

Figure 7 shows the effect of temporal regularization for three very distinct time scales, namely,  $\tau = 1, 10$  and  $100$  frames. As expected, the higher the regularization time  $\tau$ , the smaller the temporal fluctuations. In terms of displacements, the effect is quite modest, but when velocities or accelerations are aimed at, it may be convenient to use large values of  $\tau$  as long as it does not betray the occurrence of sudden events. When displacements fields are considered, the effect of changing  $\tau$  over this interval is virtually imperceptible.

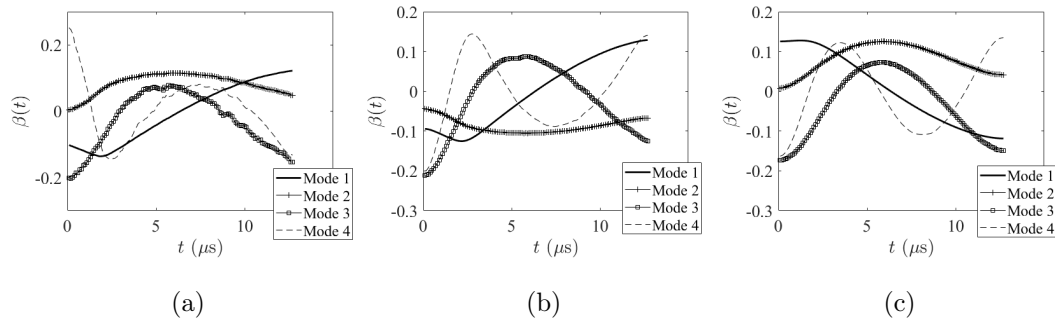


Figure 7: Four temporal modes at the last iteration for a regularization time  $\tau = 1, 10$  and 100 frames or  $\tau = 0.1, 1,$  and 10  $\mu\text{s}$ , respectively in sub-figures (a), (b) and (c)

The entire computation, dealing with the whole set of 128 images required no more than 37 seconds on a laptop computer (with single Intel i7, 3 GHz processor). A similar analysis using the same images and the same mesh but a complete set of time functions (*i.e.*, *standard* instantaneous DIC) provides very comparable results in 530 s, or 14 times longer. The displacement fields computed with the same mesh and space regularization show no detectable difference between PGD-DIC and standard (*i.e.*, global and instantaneous) DIC.

#### 4.2. 5 Mfps series

As a second test case, a similar experiment is conducted. The acquisition rate is reduced to 5 Mfps. In contrast to the previous example, the specimen remains at rest for about the first 50 frames. Then a complex multifragmentation pattern takes place. In particular, as can be seen in Figure 8(b), three parallel vertical cracks mostly oriented along the vertical direction are observed at the end of the analyzed sequence (*i.e.*, 150 images). Those cracks do not appear simultaneously, namely, a first pair emanating from the bottom contact zone initiates after the 50th frame, while a third one located between the first two appears at about the 120th frame. At the same stage, a fourth crack again vertical but located on the right side emerges from the free surface. Moreover, the

amplitude of the displacement is much larger than previously (*i.e.*, about 10 pixels for the horizontal component, or 3.6 mm). The complexity of the resulting displacement field and its non-perturbative character render this second text case much more difficult than the previous one.

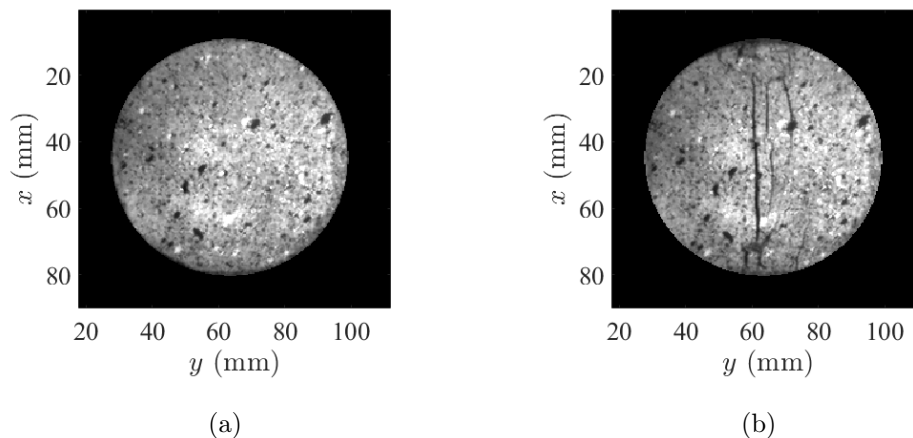


Figure 8: (a) Initial and (b) final image of the 5 Mfps series

A similar description as previously was chosen for comparison purposes. The mesh shown in Figure 9(a) is made of T3 elements with an average of 4-pixel long edges. A spatial regularization length of 20 pixels is chosen and the characteristic time  $\tau$  is equal to 10 frames (*i.e.*, 2  $\mu$ s). The same number of temporal modes  $N_m = 4$  is selected. The first four modes shown in Figure 9(b) illustrate the complex fracture scenario mentioned previously, which is to be compared with the previous case (Figure 3(b)).

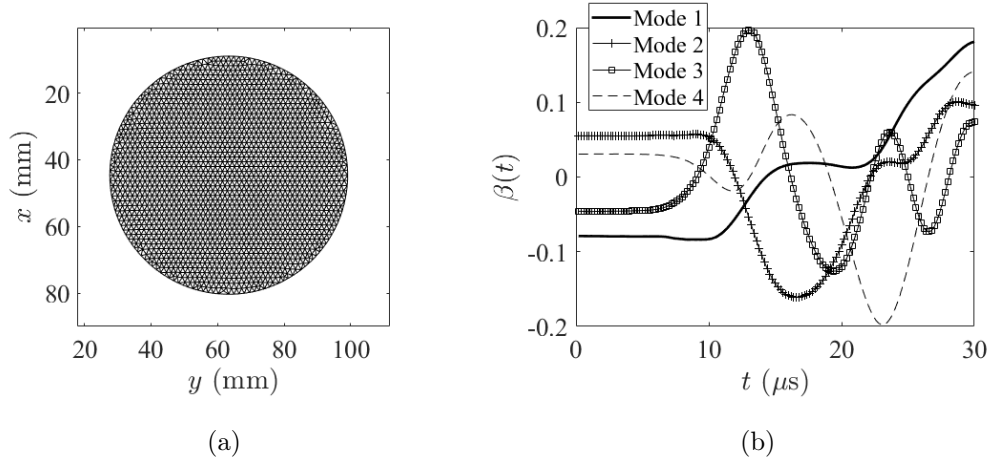


Figure 9: (a) Mesh used for the 5 Mfps series. The typical size of triangle edges is 4 pixels. (b) Time history of the four modes used at the final iteration

The displacement field at the final stage (*i.e.*, 150th frame) is shown in Figure 10. The fluctuations that can be observed along the main diameter result from the presence of the three cracks that are about 10 pixels (*i.e.*, 3.6 mm) apart on average, and the fact that the mesh has not been adjusted to allow for crack opening (although it is noteworthy that the accuracy of the residuals defined at the pixel scale, would allow the desired discontinuity to be introduced with node splitting [61, 62] or X-FEM [63] at modest cost). The crushing of contacts can also be seen in the vertical displacement, although the microstructure has not been preserved there. Such details with sharp gradient constituted a significant difficulty that was well captured.

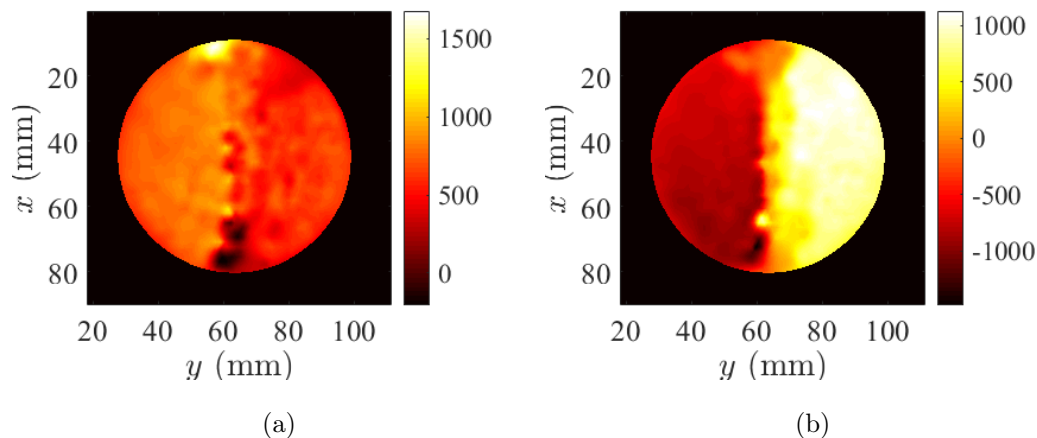


Figure 10: Displacement field (expressed in  $\mu\text{m}$ ) at the last frame (a) along the vertical  $x$  and (b) horizontal  $y$  directions for the 5 Mfps series

The gray level residuals shown in Figure 11(a) at the end of the sequence highlight very clearly the crack pattern, including the complicated fragmentation at the top contact point. The space-time cut (Figure 11(b)) also illustrates the different periods noted previously. The first still period up to time  $t \approx 10 \mu\text{s}$ , where a first crack system appears, followed by a rather calm period up to  $t \approx 24 \mu\text{s}$  where a secondary crack pattern initiates, yet opening the first crack system. Thus this active fracture period extends over about  $14 \mu\text{s}$  in real time.

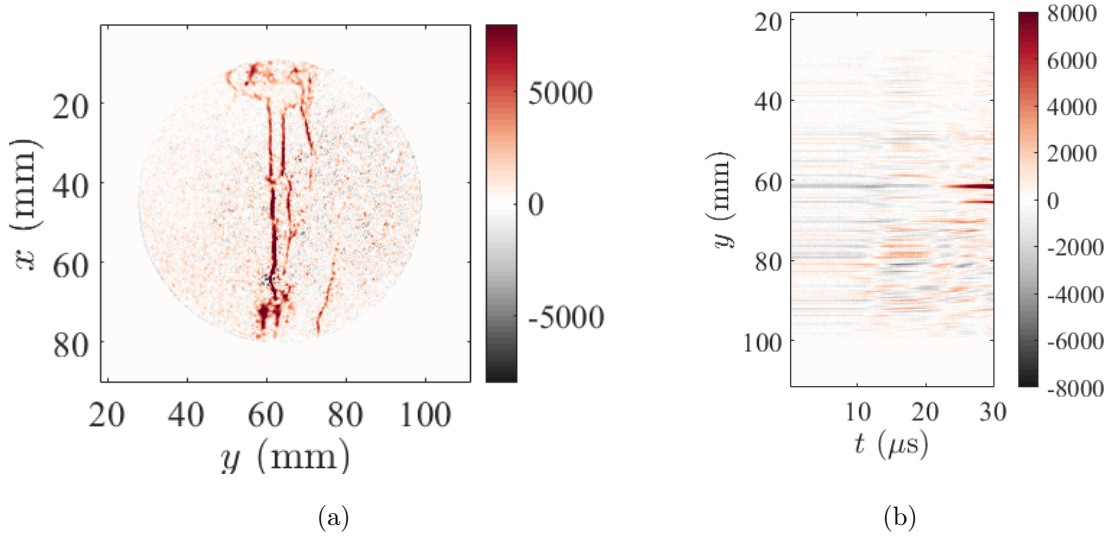


Figure 11: Gray level residual field (a) for the last frame and (b) as a space-time cut at mid  $x$  for the 5 Mfps series. The dynamic range is  $\Delta f = 38500$  gray levels

In terms of magnitude, the RMS residual amounts to 3.3 % initially but decreases down to 1.1 % after 10 iterations. At this stage, the last increment of mean displacement is less than  $10^{-6}$  pixel, thereby showing good convergence. Using 4 modes, the set of 150 frames is processed in 49 s, using the same computer as previously. Extending the number of modes to  $N_m = 16$  revealed imperceptible in terms of displacement field and residuals. The total computation time did not increase much either (53 s vs. 49 s). When compared to a complete instantaneous analysis keeping all parameters identical, which ran for 490 s, the PGD approach cuts down the computation time by one order of magnitude. The displacement fields cannot be distinguished between PGD-DIC and standard DIC provided the same mesh and space regularization is used. The time regularization does not filter out any significant part of the sample response.

## 5. Relationship with other model reduction techniques

The heart of the present approach is based on a model reduction technique accounting for a specific explanation for the time history of a stack of images. One may wonder about its relationship with a “brute-force” analysis that would consist in a direct POD of the stack of images, or more precisely of the difference of images with the reference picture (*i.e.*, the time average of the image stack). In the following, the two studied cases are reconsidered based on a simple POD of the image stack. In order not to bias the comparison a similar temporal regularization is introduced with a characteristic time  $\tau = 10$  frames (*i.e.*, 1 or 2  $\mu\text{s}$  respectively for the 10 or 5 Mfps cases). Similarly, the stack of images has been clipped to the Region of Interest that was considered in the PGD-DIC analysis.

### 5.1. 10 Mfps case

It was previously observed that mostly one temporal mode was needed in terms of kinematics (*i.e.*, axial splitting) and that the amplitude of motion was small (*i.e.*, less than a pixel). Such a small amplitude suggests that a Taylor expansion of the perturbation induced by the motion is legitimate. This observation leads to

$$\begin{aligned} f(\mathbf{x}, t) &= f(\mathbf{x}, t_0) + \mathbf{u}(\mathbf{x}, t) \cdot \nabla f(\mathbf{x}, t_0) \\ &+ \frac{1}{2}(\mathbf{u}(\mathbf{x}, t) \cdot \nabla f(\mathbf{x}, t_0))(\mathbf{u}(\mathbf{x}, t) \cdot \nabla f(\mathbf{x}, t_0)) + h.o.t. \end{aligned} \quad (24)$$

The decomposition of the displacement field into different modes coincides with a modal expansion with separated fields, thereby leading to expect a polynomial ordering of the temporal modes and gradients or higher differentials of images as the spatial modes.

This expectation is consistent with results of POD of the image stack (after subtraction of the reference picture). Figure 12(a) shows that the eigenvalues of the decomposition drop extremely fast after the first one, and more than two orders of

magnitude are lost for the third mode, and about three orders of magnitude for the fourth one. This result is consistent with the number of modes used in the previous analysis. The temporal modes of Figure 12 show that the first one is mostly linear, and low order polynomials are needed to fit the following ones.

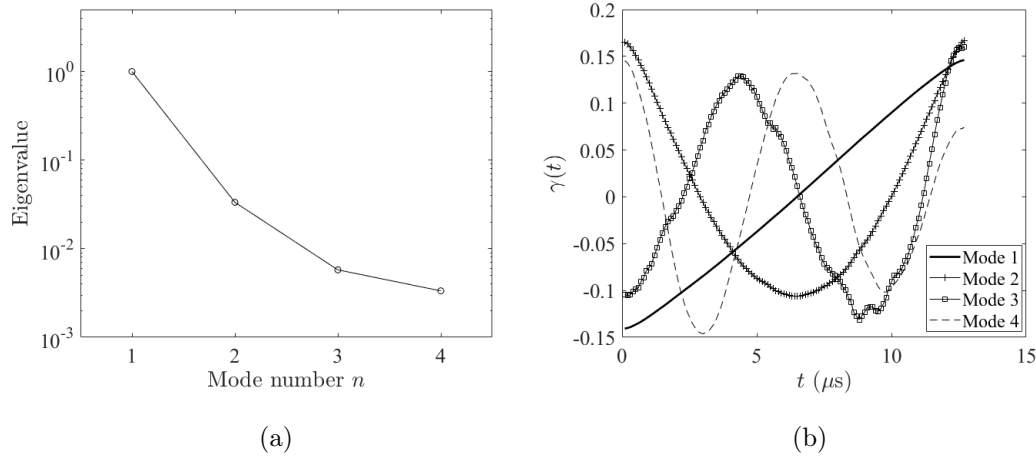


Figure 12: (a) Semi-log plot of the eigenvalues of the temporal modes (normalized to the first one) for the 10 Mfps series. (b) First four temporal modes

In terms of spatial modes, as suggested by the previous argument, the first mode is easily interpreted as the dominant kinematic mode. The opening of the two specimen halves with a rotation point close to the top contact is read from the “false relief” pattern (Figure 13(a)). The other modes are much more difficult to interpret, consistently with the fact that they have to involve higher order derivatives of the image (with higher frequencies). However details of the main and secondary cracks are visible in mode 2 (Figure 13(b)), and further modes seem to bring some features close to the contact points (Figure 13(c-d)).



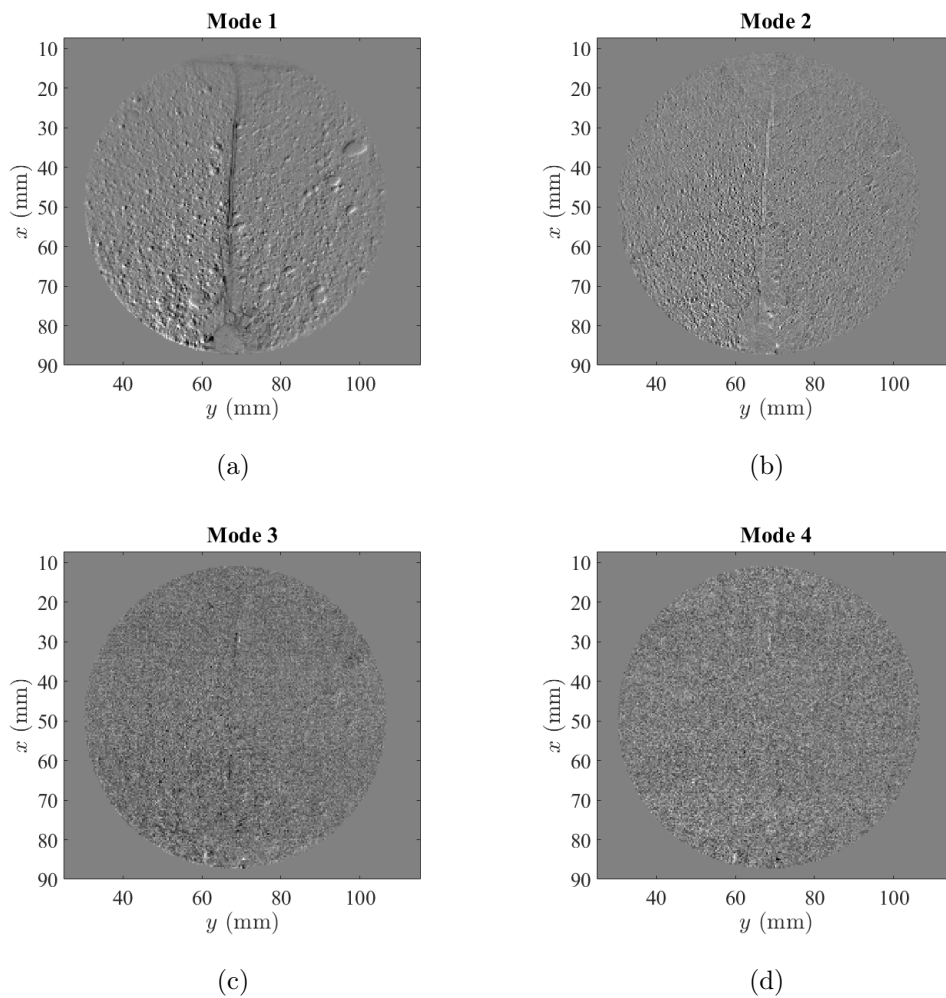


Figure 13: Spatial modes for the 10 Mfps series. The first mode is easily interpreted in terms of displacement. The following ones provide an enrichment to the description close to cracks and contact points

Thus, it appears that the intrinsic information captured by the “brute force” analysis and PGD-DIC are very close. PGD-DIC is more naturally interpreted as due to displacements, because they are the starting postulate, but intrinsically it appears that the information content is very close.

### 5.2. 5 Mfps case

The 5 Mfps case revealed a much more complex kinematics (Figures 9 and 10), and that the amplitude of motion was much more extended. Yet four modes were sufficient to analyze the image series composed of 150 images. The mere fact that the amplitude of motion is large (*i.e.*, about 10 pixels or 3.6 mm) and that the contrast of images is very short range correlated means that even in the extremely simplistic case of, say, a uniform velocity in space and time, 10 different images (each translated by one pixel) would be needed to capture the motion. Heterogeneity in space and time makes the description even more demanding. Additionally, a smooth subpixel interpolation (by cubic splines) was used in PGD-DIC rather than linear subpixel interpolation. This choice increases further the number of required independent fields.

Following the same reasoning as previously, it is shown in Figure 14(a) that the complexity of the image stack is higher, in the sense that the decay of eigenvalues is much slower than previously (Figure 12(a)), less than two decades for the fourth mode relative to the first one. The temporal modes (Figure 14(b)) show in a less pronounced way the two episodes of cracking that are very clearly read from the first mode in Figure 9(b).

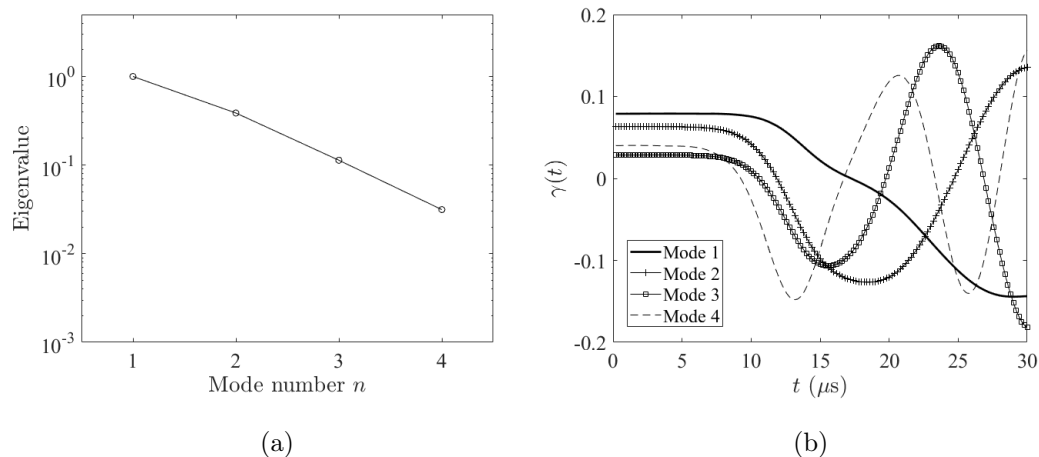


Figure 14: (a) Semi-log plot of the eigenvalues of the temporal modes (normalized to the first one) for the 5 Mfps series. (b) First four temporal modes

The first four spatial modes given in Figure 15(a-d) show that strong spatial correlations are present even in the fourth mode. This observation demonstrates that the information content is still far from being exhausted with these four modes and much more would be needed to reach the quality of the interpretation provided by PGD-DIC.

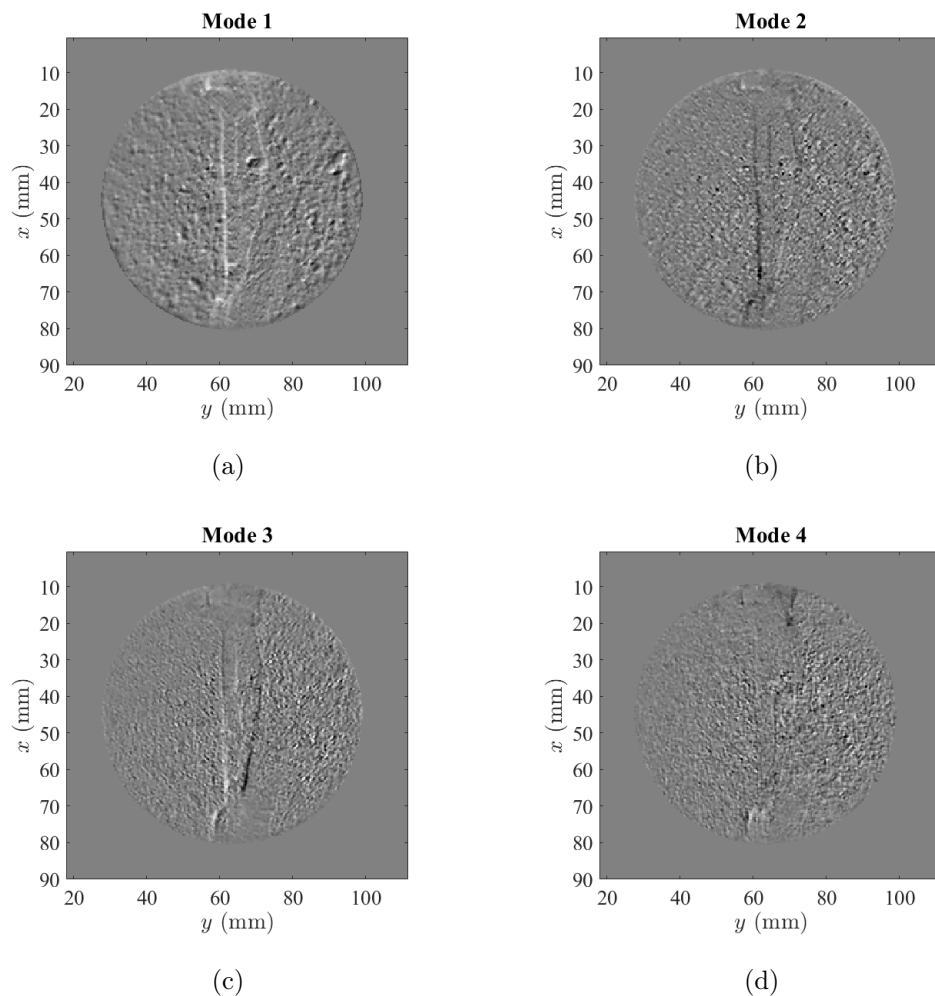


Figure 15: Spatial modes for the 5 Mfps series. The first mode is easily interpreted in terms of displacement, but the following ones are more difficult to analyze

For this second (and more complex) example, the nonlinear transformation associated with a large motion has been incorporated in the DIC analysis and hence the motion interpretation of the origin of the image difference allows us to have a much more suited model reduction based on the observed motion, rather than the images themselves. Not only is DIC registration more accurate by being more faithful to reality, but it also allows for a further simplicity of interpretation.

This section highlights the fact that physical motion (although complex and

containing propagating discontinuities) may be very fruitfully exploited by a modal analysis, namely, PGD tailored to DIC, whereas the manifestation of this motion read in the stack of images may reveal even more complex calling for much more information. Images and motions share the same “complexity” only in the limit of very small motion amplitudes and large spatial correlations.

## 6. Conclusion

This paper has introduced a (simple) methodology based on PGD suited to DIC analyses. The spirit of the approach is very close to what was proposed initially for 2D and 3D spatial dimensions [39, 40] and further extended very recently to space and time [48, 41], as in the present study. The latter appears to be very prone to the separation of modes into space and time fields.

It is worth noting that this space and time separation with a similar PGD analysis was also already used [48] in the more complex framework of tomography, where only some projections are available. This last feature introduced numerous subtle changes that made the reduction to the 2D case not transparent. In particular, the perfect decoupling of space and time was not present in the above reference due to the incomplete spatial information contained in a single projection.

The main novel contributions of the present study can be listed as follows:

- A full PGD approach to DIC has been proposed including an arbitrary number of modes. Although this may appear as a technical detail, let us emphasize that the simultaneous determination of several modes turns out to be much more efficient than the successive determination of a single mode as proposed in Ref. [41], since residuals may saturate to a nontrivial field that cannot be explained by a

displacement and hence that are not reduced over iterations.

- The PGD-DIC approach was shown to be fully compatible with space and time *regularizations* enforcing mechanical admissibility and smoothness, respectively. The temporal regularization takes here the form of a non trivial change of basis issued from the regularized metric for the determination of the temporal modes. This appears to be quite general and can be used in a much broader framework.
- It was shown that the complexity of full time series reduces to the cost of a very few (*i.e.*, the number of modes) global analyses. Moreover, the change from instantaneous and global DIC analyses to the present PGD framework represents few tens of lines of matlab code, and can be made non-intrusive. Similarly, the proposed modal decomposition can easily be implemented in a non-intrusive approach if a commercial DIC software is available.
- The reference state used in the present study could have been the first image as usually performed in classical DIC. However, the choice was made to compute a “denoised” reference image that is progressively extracted from the image series as the kinematics is progressively determined and accounted for. In a more general framework, this procedure for computing the reference state is optimal.
- The proposed formalism is not only of low intrusiveness, but also reveals very powerful in terms of computational efficiency. In the considered examples, the computation time was cut down by a factor 10-15 as compared to instantaneous DIC.
- On a theoretical ground, the connection of the proposed approach with a simple POD of the full image stack was clarified. Both were shown to be identical in the limit of a vanishing displacement amplitude, but much more robustness and

data soberness was obtained using the proposed PGD-DIC approach for large displacements as a result of nonlinearities involved in translating displacements into gray level changes.

- Ultra-fast imaging videos up to 10 Mfps from dynamic Brazilian tests performed on concrete specimens were used as test cases. In spite of these exceptionally high speeds, the image quality revealed remarkably good. No more than four modes were needed to perform the analysis (in less than one minute for stacks of 128 and 150 images).

### *Acknowledgments*

This work was partly supported under PRC MECACOMP, French research project co-funded by DGAC and SAFRAN Group, headed by SAFRAN Group and involving SAFRAN Group, ONERA and CNRS. It is a pleasure to acknowledge useful discussions with Rana Akiki, Bastien Durand, Fabrice Gatuingt, Jean-Louis Lafoeste and Bumedijen Raka.

### **References**

- [1] M. Sutton, J. Orteu, H. Schreier, Image correlation for shape, motion and deformation measurements: Basic Concepts, Theory and Applications, Springer, New York, NY (USA), 2009.
- [2] F. Hild, S. Roux, Digital image correlation, in: P. Rastogi, E. Hack (Eds.), Optical Methods for Solid Mechanics. A Full-Field Approach, Wiley-VCH, Weinheim (Germany), 2012, pp. 183–228.
- [3] M. Sutton, Computer vision-based, noncontacting deformation measurements in mechanics: A generational transformation, Appl. Mech. Rev. 65 (AMR-13-1009) (2013) 050802.
- [4] X. Hu, S. Palmer, J. Field, The application of high speed photography and white light speckle to the study of dynamic fracture, Optics Lasers Technol. 16 (6) (1984) 303–306.

- [5] J. Huntley, S. Palmer, J. Field, Automatic speckle photography fringe analysis: Application to crack propagation and strength measurement, *Proc. SPIE* 0814 (1987) 153–160.
- [6] B. Asay, G. Laabs, B. Henson, D. Funk, Speckle photography during dynamic impact of an energetic material using laser-induced fluorescence, *J. Appl. Phys.* 82 (3) (1997) 1093–1099.
- [7] W. Peters, W. Ranson, J. Kalthoff, S. Winkler, A study of dynamic near-crack-tip fracture parameters by digital image analysis, *J. Phys. Coll.* 46 (C5) (1985) 631–638.
- [8] F. Barthelat, Z. Wu, B. Prorok, H. Espinosa, Dynamic torsion testing of nanocrystalline coatings using high-speed photography and digital image correlation, *Exp. Mech.* 43 (3) (2003) 331–340.
- [9] J. Kajberg, M. Sjödaahl, Optical method to study material behaviour at high strain rates, in: P. Stähle, K. Sundin (Eds.), *IUTAM Symposium on Field Analyses for Determination of Material Parameters – Experimental and Numerical Aspects*, Vol. 109 of *Solid Mechanics and its Applications*, Springer (the Netherlands), 2003, pp. 37–49.
- [10] I. Elnasri, S. Pattofatto, H. Zhao, H. Tsitsiris, F. Hild, Y. Girard, Shock enhancement of cellular structures under impact loading: Part i experiments, *J. Mech. Phys. Solids* 55 (2007) 2652–2671.
- [11] J. Kajberg, B. Wikman, Viscoplastic parameter estimation by high strain-rate experiments and inverse modelling – speckle measurements and high-speed photography, *Int. J. Solids Struct.* 44 (1) (2007) 145–164.
- [12] V. Tarigopula, O. Hopperstad, M. Langseth, A. Clausen, F. Hild, A study of localisation in dual phase high-strength steels under dynamic loading using digital image correlation and fe analysis, *Int. J. Solids Struct.* 45 (2) (2008) 601–619.
- [13] F. Pierron, M. Sutton, V. Tiwari, Ultra high speed dic and virtual fields method analysis of a three point bending impact test on an aluminium bar, *Exp. Mech.* 51 (4) (2011) 537–563.
- [14] D. Saletti, S. Pattofatto, H. Zhao, Measurement of phase transformation properties under moderate impact tensile loading in a niti alloy, *Mech. Mat.* 65 (2013) 1–11.
- [15] F. Hild, A. Bouterf, P. Forquin, S. Roux, On the Use of Digital Image Correlation for the Analysis of the Dynamic Behavior of Materials, in: *The Micro-World Observed by Ultra High-Speed Cameras*, 2018, pp. 185–206.
- [16] B. Lucas, T. Kanade, An iterative image registration technique with an application to stereo vision, in: *7th International Joint Conference on Artificial Intelligence*, 1981, pp. 674–679.
- [17] W. Peters, W. Ranson, Digital imaging techniques in experimental stress analysis, *Opt. Eng.* 21



- (1982) 427–431.
- [18] M. Sutton, W. Wolters, W. Peters, W. Ranson, S. McNeill, Determination of displacements using an improved digital correlation method, *Im. Vis. Comp.* 1 (3) (1983) 133–139.
- [19] B. Wagne, S. Roux, F. Hild, Spectral approach to displacement evaluation from image analysis, *Eur. Phys. J. AP* 17 (2002) 247–252.
- [20] G. Broggiato, Adaptive image correlation technique for full-field strain measurement, in: C. Pappalettere (Ed.), *12th Int. Conf. Exp. Mech.*, McGraw Hill, Lilan (Italy), 2004, pp. 420–421.
- [21] Y. Sun, J. Pang, C. Wong, F. Su, Finite-element formulation for a digital image correlation method, *Appl. Optics* 44 (34) (2005) 7357–7363.
- [22] G. Besnard, F. Hild, S. Roux, “Finite-element” displacement fields analysis from digital images: Application to Portevin-Le Chatelier bands, *Exp. Mech.* 46 (2006) 789–803.
- [23] H. Leclerc, J. Périé, S. Roux, F. Hild, Integrated digital image correlation for the identification of mechanical properties, Vol. LNCS 5496, Springer, Berlin (Germany), 2009, pp. 161–171.
- [24] F. Mathieu, H. Leclerc, F. Hild, S. Roux, Estimation of elastoplastic parameters via weighted FEMU and integrated-DIC, *Exp. Mech.* 55 (1) (2015) 105–119.
- [25] A. Chatterjee, An introduction to the proper orthogonal decomposition, *Current Science* 78 (7) (2000) 808–817.
- [26] A. Antoranz, A. Ianiro, O. Flores, M. García-Villalba, Extended proper orthogonal decomposition of non-homogeneous thermal fields in a turbulent pipe flow, *International Journal of Heat and Mass Transfer* 118 (DOI: 10.1016/j.ijheatmasstransfer.2017.11.076) (2018) 1264–1275.
- [27] A. Benaarbia, A. Chrysochoos, Proper orthogonal decomposition preprocessing of infrared images to rapidly assess stress-induced heat source fields, *Quantitative InfraRed Thermography Journal* 14 (DOI: 10.1080/17686733.2017.1281553) (2017) 132–152.
- [28] S. R. Kalidindi, *Hierarchical Materials Informatics - Novel Analytics for Materials Data*, Elsevier, Oxford (UK), 2015.
- [29] M. F. Mohamed, A.-R. Shabayek, M. El-Gayyar, H. Nassar, An adaptive framework for real-time data reduction in ami, *Journal of King Saud University - Computer and Information Sciences* (in press).
- [30] H. Strasdat, J. Montiel, A. J. Davison, Visual slam: Why filter?, *Image and Vision Computing*

- 30 (DOI: 10.1016/j.imavis.2012.02.009) (2012) 65–77.
- [31] A. Charbal, S. Roux, F. Hild, L. Vincent, Spatiotemporal regularization for digital image correlation: Application to infrared camera frames, *Int. J. Num. Meth. Eng.*
- [32] F. Chinesta, A. Ammar, E. Cueto, Recent advances and new challenges in the use of the proper generalized decomposition for solving multidimensional models, *Arch. Comput. Meth. Eng.* 17 (4) (2010) 327–350.
- [33] A. Nouy, Proper generalized decompositions and separated representations for the numerical solution of high dimensional stochastic problems, *Archives of Computational Methods in Engineering* 17 (4) (2010) 403–434.
- [34] P. Ladevèze, *Nonlinear computational structural mechanics: new approaches and non-incremental methods of calculation*, Springer Science & Business Media, 2012.
- [35] P. Ladevèze, PGD in linear and nonlinear computational solid mechanics, in: *Separated Representations and PGD-Based Model Reduction*, Springer, 2014, pp. 91–152.
- [36] T. Cormen, *Introduction to algorithms*, 3rd Edition, MIT press, 2009.
- [37] D. González, A. Badiás, I. Alfaro, F. Chinesta, E. Cueto, Model order reduction for real-time data assimilation through extended kalman filters, *Comput. Methods Appl. Mech. Engrg.* 326 (DOI: 10.1016/j.cma.2017.08.041) (2017) 679–693.
- [38] E. Nadal, F. Chinesta, P. Díez, F. Fuenmayor, F. Denia, Real time parameter identification and solution reconstruction from experimental data using the proper generalized decomposition, *Comput. Methods Appl. Mech. Engrg.* 296 (DOI: 10.1016/j.cma.2015.07.020) (2015) 113–128.
- [39] J. Passieux, J. Périé, Digital image correlation using proper generalized decomposition: PGD-DIC, *Int. J. Num. Meth. Eng.* 92 (6) (2012) 531–550.
- [40] L. G. Perini, J.-C. Passieux, J.-N. Périé, A multigrid PGD-based algorithm for volumetric displacement fields measurements, *Strain* 50 (4) (2014) 355–367.
- [41] J.-C. Passieux, R. Bouclier, J. N. Périé, A Space-Time PGD-DIC Algorithm: Application to 3D Mode Shapes Measurements, *Exp. Mech.* doi:10.1007/s11340-018-0387-2.
- [42] J. Neggers, O. Allix, F. Hild, S. Roux, *Big Data in Experimental Mechanics and Model Order Reduction: Today’s Challenges and Tomorrow’s Opportunities*.
- [43] S. Roux, F. Hild, Stress intensity factor measurements from digital image correlation: post-processing and integrated approaches, *Int. J. Fract.* 140 (1-4) (2006) 141–157.

- [44] F. Hild, S. Roux, Digital image correlation: From measurement to identification of elastic properties - a review, *Strain* 42 (2006) 69–80.
- [45] P. Ladevèze, Sur une famille d’algorithmes en mécanique des structures, *C. R. Acad. Sci.* 300 (IIb) (1985) 41–44.
- [46] G. Besnard, H. Leclerc, S. Roux, F. Hild, Analysis of image series through digital image correlation, *J. Strain Analysis* 47 (4) (2012) 214–228.
- [47] M. Berny, T. Archer, A. Mavel, P. Beauchêne, S. Roux, F. Hild, On the analysis of heat haze effects with spacetime DIC, *Opt. Lasers Eng.* (DOI: 10.1016/j.optlaseng.2018.06.004).
- [48] C. Jailin, A. Buljac, A. Bouterf, M. Poncelet, F. Hild, S. Roux, Self-calibration for lab- $\mu$ ct using space-time regularized projection-based dvc and model reduction, *Meas. Sci. Technol.* 29 (2018) 024003.
- [49] A. Buljac, C. Jailin, A. Mendoza, T. Taillandier-Thomas, A. Bouterf, J. Neggers, B. Smaniotto, F. Hild, S. Roux, Digital volume correlation: Review on progress and challenges, *Exp. Mech.* (in press).  
URL <http://doi.org/10.1007/s11340-018-0390-7>
- [50] P. Boisse, P. Bussy, P. Ladevèze, A new approach in non-linear mechanics: The large time increment method, *Int. J. Num. Meth. Eng.* 29 (3) (1990) 647–663.
- [51] P. Ladevèze, J.-C. Passieux, D. Néron, The latin multiscale computational method and the proper generalized decomposition, *Comput. Meth. Appl. Mech. Eng.* 199 (21) (2010) 1287–1296.
- [52] A. Tikhonov, V. Arsenin, *Solutions of ill-posed problems*, J. Wiley, New York (USA), 1977.
- [53] G. Broggiato, L. Casarotto, Z. Del Prete, D. Maccarrone, Full-field strain rate measurement by white-light speckle image correlation, *Strain* 45 (4) (2009) 364–372.
- [54] D. Claire, F. Hild, S. Roux, A finite element formulation to identify damage fields: The equilibrium gap method, *Int. J. Num. Meth. Engng.* 61 (2) (2004) 189–208.
- [55] J. Réthoré, S. Roux, F. Hild, An extended and integrated digital image correlation technique applied to the analysis fractured samples, *Eur. J. Comput. Mech.* 18 (2009) 285–306.
- [56] Z. Tomičević, F. Hild, S. Roux, Mechanics-aided digital image correlation, *J. Strain Analysis* 48 (2013) 330–343.
- [57] F. Lobo Carneiro, Um novo método para determinação da resistência à tração dos concretos, in: *Anais 5a reunião da Associação Brasileira de Normas Técnicas (ABNT) em São Paulo, 1943*,

pp. 127–129.

- [58] F. Lobo Carneiro, Une nouvelle méthode pour la détermination de la résistance à la traction des bétons, *Bull. RILEM* 13 (1953) 103–108.
- [59] H. Kolsky, An investigation of the mechanical properties of materials at very high rates of loading, *Proc. Phys. Soc. London* 62b (1949) 676–700.
- [60] R. Akiki, Développement d’un outil numérique pour la prévision de la fissuration d’une structure en béton de fibres sous impact, PhD thesis (in French), Paris-Saclay University (France), <https://tel.archives-ouvertes.fr/tel-01708295> (2017).
- [61] S. Roux, F. Hild, H. Leclerc, Mechanical assistance to dic, in: H. Espinosa, F. Hild (Eds.), *Full field measurements and identification in Solid Mechanics*, Vol. *Procedia IUTAM*, 4, Elsevier, 2012, pp. 159–168.
- [62] E. Fagerholt, T. Børvik, O. S. Hopperstad, Measuring discontinuous displacement fields in cracked specimens using digital image correlation with mesh adaptation and crack-path optimization, *Optics Lasers Eng.* 51 (3) (2013) 299–310.
- [63] J. Réthoré, F. Hild, S. Roux, Extended digital image correlation with crack shape optimization, *Int. J. Num. Meth. Eng.* 73 (2) (2008) 248–272.